Opto-Electronic Engineering

Article

2017, Vol 44, Issue 11

A differential-imaging polarimeter for high-contrast exoplanet imaging

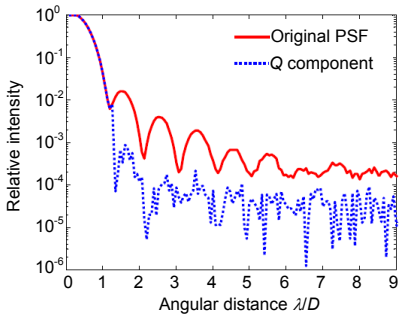

Deqing Ren[1,2,3], Chao Yang[2,3,4]*, Jing Guo[2,3] and Chengchao Liu[2,3]

[1]Physics & Astronomy Department, California State University Northridge, Northridge 91330, USA; [2]National Astronomical Observatories/Nanjing Institute of Astronomical Optics & Technology, Chinese Academy of Sciences, Nanjing 210042, China; [3]Key Laboratory of Astronomical Optics & Technology, Nanjing Institute of Astronomical Optics & Technology, Chinese Academy of Sciences, Nanjing 210042, China; [4]University of Chinese Academy of Sciences, Beijing 100049, China

Abstract: Starlight is generally unpolarized, but the light reflected from the planet is linearly polarized as the result of the Rayleigh scattering. For ground-based exoplanet imaging, atmospheres turbulence is changing from time to time, which induces speckle noise and hampers the high-contrast imaging of the faint exoplanets. In this paper, we propose a differential-imaging polarimeter dedicated for exoplanet high-contrast imaging. The system contains a zero-order half-wave plate (HWP) located on the optical pupil plane, which can rotate to modulate the incoming light, and a Wollaston prism (WP) is used to generate two polarized images, which is used for simultaneously polarization differential imaging and thus our system is fundamentally immune to the atmospheric turbulence induced temporally-variable wavefront aberration. Our polarimeter can be inserted near the telescope image focal plane, and provide an extra contrast for the exoplanet high-contrast imaging. To achieve best differential-imaging performance, dedicated algorithm is developed, which can effectively correct the distortion and the intensity unbalance between the two differential images. The system successfully achieves an extra contrast of ~30~50 times, which can be used with current adaptive optics and coronagraph system for directly imaging of giant Jupiter-like exoplanets.

Keywords: polarimeter; high-contrast imaging; half-wave plate

DOI: 10.3969/j.issn.1003-501X.2017.11.002 **Citation:** *Opto-Elec Eng*, 2017, **44**(11): 1045−1051

1 Introduction

Over the past two decades, the detection of exoplanets is one of the most important research topics in astronomy [1-4], and until now, more than 3600 exoplanets have been detected by using different methods (http://exoplanet.eu/). Different from the indirect method, the direct imaging, which directly captures photons from an exoplanet, is a very promising technique and a basic required technique for searching extraterrestrial life signals, since it can provide spectroscopic information, which can be used to analyze exoplanet atmospheric composites and the signs of biomarker. However, the direct imaging of exoplanets is an extremely challenging technique, because of the close angular separation and high contrast ratio between a planet and its primary star. Traditionally, some high-contrast imaging techniques, such as high-contrast coronagraphs or dark holes generated by controlling the wavefront, are employed to suppress the star light in order to extract the planet photons [5-11]. However, each technique has its own limitation. For example, the dark-hole approach can only generate a high contrast in a small discovery area [12,13], while a coronagraph is very sensitive to the wavefront error, which limits its performance not better than 10^{-7} for a ground observation [14]. All the current high-contrast techniques are suffered from the atmospheric turbulence induced wavefront aberration, which changes rapidly from time to time and thus induces the so-called speckle noise, making high-contrast imaging with a ground-based telescope extremely difficult. Therefore, developing a novel method to improve the imaging contrast is an urgent issue.

Studies have shown that light reflected from the exoplanet is normally linearly polarized and the direct light from the star is in general unpolarized [15-18]. Thus, a polarimeter can be employed to reduce the influence of speckles and enhance the exoplanet imaging contrast [19-24]. Currently, some polarimeters dedicated for exopla-

Received 12 August 2017; accepted 20 October 2017
* E-mail: chaoyang@niaot.ac.cn

nets imaging have been developed for ground-based telescopes, such as the Gemini planet imager (GPI) and spectro-polarimetric high-contrast exoplanet research instrument (SPHERE), which are able to deliver a total contrast of 10^{-6}~10^{-7} when working with coronagraphs. In the SPHERE, to overcome the rapidly-changed atmospheric turbulence induced speckle noise, a special manufactured CCD camera, including a special mask and a micro lenslet array, must be used to synchronize with the ferroelectric liquid crystals at extremely high-speed [25]. Until now, no polarimeter has been successfully used for exoplanet imaging, although they are being used for the less challenging polarization measurements of the star debris disks and associated structures[26].

According to star-exoplanet theoretical modeling, to image a giant Jupiter-like exoplanet, a contrast of 10^{-8} or better is required at a close angular distance [27, 28]. Current-generation extreme adaptive optics and coronagraph combination systems with 8-meter class telescopes, such as Gemini, VLT and Subaru, aim to achieve a contrast of 10^{-7} [29-31], and up to ~$10^{-6.5}$ contrast is achieved [32,33]. Therefore, it is critical if an extra contrast of 10^{-1} or better can be provided by a dedicated instrument, which can be integrated into future extreme adaptive optics and coronagraph system for such ground-based high-contrast imaging. To attack this rapidly-changed atmospheric induced speckle noise and provide an extra contrast for such critical scientific goal, we propose a differential-imaging polarimeter dedicated for exoplanet imaging, which is composed of a half-wave plate and a Wollaston prism, and each polarization component (Q or U) can be measured simultaneously, and thus it is fundamentally immune to the atmospheric turbulence. Our polarimeter is simple and compact, which can be easily integrated into an adaptive optics and coronagraph system to measure the Stokes parameters I, Q and U. To achieve the best performance, an eight-variable parameter optimization algorithm was proposed to correct possible image distortion and intensity unbalance in the polarimeter system. Here, we discuss the instrument design, principle and data reduction algorithm in Section 2. In Section 3, the laboratory test results are discussed. Conclusions and future work are presented in Section 4.

2 Differential-imaging polarimeter

2.1 Principle and methodology

Figure 1 depicts the working principle of the differential-imaging polarimeter, which consists of a collimator lens, a half-wave plate (HWP), a Wollaston prism (WP), an image lens and a CCD camera. In Fig. 1, only the on-axis starlight is shown. The incoming light from the telescope focus is first collimated by the collimator lens, and then it is modulated by the half-wave plate and the Wollaston prism, and finally formed on the imaging on the focal plane of the CCD camera.

According to the system layout and Mueller calculus, the relationship between input and output Stokes vectors, $\boldsymbol{S}_{\text{in}}$ and $\boldsymbol{S}_{\text{out}}$ is given by:

$$\boldsymbol{S}_{\text{out}} = \boldsymbol{M}_{\text{WP}} \cdot \boldsymbol{M}_{\text{HWP}} \cdot \boldsymbol{S}_{\text{in}}, \tag{1}$$

where $\boldsymbol{M}_{\text{HWP}}$ and $\boldsymbol{M}_{\text{WP}}$ are Mueller matrices of the half-wave plate and the Wollaston prism respectively, which can be expressed by Eqs. (2) and (3). α is azimuth angle of fast axis of the half-wave plate, δ is its retardance, and β is the azimuth angle of transmission axis of the Wollaston prism.

$$\boldsymbol{M}_{\text{HWP}}(\alpha,\delta) = \begin{bmatrix} 1 & 0 & 0 & 0 \\ 0 & \cos^2 2\alpha + \sin^2 2\alpha\cos\delta & \cos 2\alpha \sin 2\alpha(1-\cos\delta) & -\sin 2\alpha \sin\delta \\ 0 & \cos 2\alpha \sin 2\alpha(1-\cos\delta) & \sin^2 2\alpha + \cos^2 2\alpha\cos\delta & \cos 2\alpha \sin\delta \\ 0 & \sin 2\alpha \sin\delta & -\cos 2\alpha \sin\delta & \cos\delta \end{bmatrix}, \tag{2}$$

$$\boldsymbol{M}_{\text{WP}}(\beta) = \frac{1}{2}\begin{bmatrix} 1 & \cos 2\beta & \sin 2\beta & 0 \\ \cos 2\beta & \cos^2 2\beta & \cos 2\beta \sin 2\beta & 0 \\ \sin 2\beta & \cos 2\beta \sin 2\beta & \sin^2 2\beta & 0 \\ 0 & 0 & 0 & 0 \end{bmatrix}, \tag{3}$$

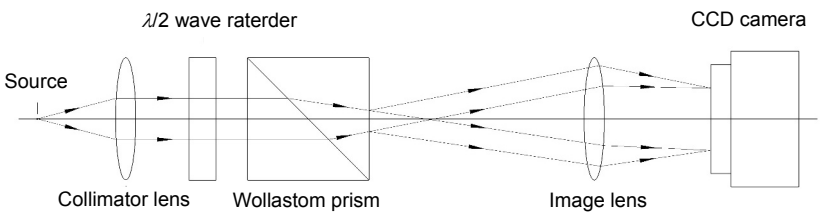

Fig. 1 Schematic of the working principle of the differential-imaging polarimeter.

Two images are generated simultaneously by the Wollaston prism, which are perpendicular in linear polarized status. We assume one image is in the X linear polarization direction (called I_L, i.e. the left side image), while the other one is in the Y linear polarization direction (called I_R, i.e. the right side image). By carefully chosen $\beta = 0°$, $\alpha = 0°$ and $\alpha = 22.5°$ (with X-axis respectively), and $\delta = \pi$, the Stoke components of the I, Q and U can be derived from Eqs. (4)~(6) as:

$$I = I_L(0) + I_R(0), \tag{4}$$

$$Q = I_L(0) - I_R(0), \tag{5}$$

$$U = I_L(22.5°) - I_R(22.5°), \tag{6}$$

where I is the overall intensity, and Q and U are two linear components. Therefore, the proposed polarimeter can retrieve Q or U component simultaneously, that is, when the half-wave plate axis is aligned in X-axis, the subtraction of the left side image with that of the right side yields the Q component, while when the half-wave plate axis is aligned in the direction that has an angle of 22.5° with X-axis, the subtraction yields the U component. In such a way, the unpolarized starlight, including the induced speckle noise, is subtracted in each subtraction in Eq. (5) or Eq. (6), and only the polarized exoplanet light is kept. Accordingly, the overall polarized exoplanet image can be calculated as:

$$P = \sqrt{U^2 + Q^2}. \tag{7}$$

2.2 One-subtraction algorithm

Assume star image is located on axis, while the exoplanet image is located on off-axis of the telescope image plane. For the star image is much brighter than that of the exoplanet, the exoplanet image cannot be seen before the polarimeter. Since starlight is in generally unpolarized, while exoplanet light is somehow polarized, we will focus our discussions on the subtraction of the on-axis starlight, which will automatically result in an extraction of the polarized exoplanet light. However, the direction subtraction of the left side and right side images by using Eq. (5) or Eq. (6) cannot yield a good result. For example, the intensity difference in both side beams limits the performance of such subtraction. In addition, the image distortion, which will result in a difference for the star point spread functions (PSFs) on both sides, will also seriously limit the subtraction. Therefore, the Q and U extraction based on the above equations can be significantly improved, if such intensity unbalance and distortion can be corrected.

To address these issues, firstly we consider three image distortions: radial distortion, decentering distortion and thin prism distortion, since these kinds of distortions exist widely in the imaging systems. Although distortions do not affect the image sharpness, they have influence on the precision of image positions, which will degrade the performance of image subtraction from the two polarization arms consequently [34,35]. Several distortion correction methods were developed by the researchers [36-39] for imaging purpose, not for polarization subtraction. For the best subtraction, we propose an optimization approach. In this case, the coordinate (x_d, y_d) in the original image will be corrected as the corresponding coordinate (x_u, y_u) on the corrected image as:

$$x_u = x_d + (g_1 + g_3)x_d^2 + g_4 x_d y_d + g_1 y_d^2 + g_5 x_d (x_d^2 + y_d^2), \tag{8}$$

$$y_u = y_d + (g_1 + g_4)y_d^2 + g_3 x_d y_d + g_2 x_d^2 + g_5 x_d (x_d^2 + y_d^2). \tag{9}$$

In our optimization approach, five variables (g_1, g_2, g_3, g_4 and g_5) need to be optimized in the above equations. The distortions need only to be corrected on one image, until both images are identical and have best subtraction. Here we assume the right side image is corrected. In addition, the two images also need to be aligned accurately until they are exactly overlapped for the best subtraction.

Furthermore, central coordinates of the distortions x_0 and y_0, and intensity factor s are also included in the optimization, so we have eight variable parameters (g_1, g_2, g_3, g_4, g_5, x_0, y_0 and s) that will be used for optimization. For the subtraction of the left and right starlight images, the optimization is to find the minimum of sum of the absolute subtraction values of all pixels on the focal plane for the starlight PSFs (objective function) as:

$$O = \min \sum | PSF_L - PSF_R(g_1, g_2, g_3, g_4, g_5, x_0, y_0, s) |, \tag{10}$$

where only the right side image or PSF is used for image distortion and intensity unbalance corrections.

Finally, Eq. (10) can be applied to Eqs. (5) and (6) to extract the linear components Q and U, respectively. Since aberration or speckle noise induced by atmosphere is viewed as non-polarized light and is identical in the left and right channels, it will be subtracted automatically in our optimization process, and thus our polarimeter is fundamentally immune to this seeing induced aberration or speckle noise.

In the above subtraction, the objective function is to be optimized for the minimum of the starlight PSF subtraction, this means that the starlight is unnecessary to be unpolarized[40]. In fact, when the starlight has some polarization (such as a few percentage), our subtraction of Eq. (9) will yield the polarization difference between the starlight and exoplanet light.

3 Laboratory testing

3.1 Experimental setup

In the laboratory, a He-Ne laser (λ=632.8 nm) is used as a light source to simulate the unpolarized starlight. A zero-order half-wave plate (HWP, @632.8 nm) and a Wollaston prism (WP, with separation angle of 1° and extinction ratio>10^4:1 in the range 400 nm to 2 μm), both manufactured by Thorlabs, are employed as the polariza-

tion modulator and the dual-beam analyzer, respectively. A 16-bit CCD camera (1536 pixels×1024 pixels and a pixel size of 9.0 μm×9.0 μm) manufactured by SBIG records the modulated intensities. Focal lengths of the collimator lens and re-imaging lens are 800 mm and 400 mm, respectively. The experimental setup of our differential-imaging polarimeter is shown in Fig. 2.

Based on the one-subtraction algorithm presented in Sec. 2, different polarization components are retrieved using Eqs. (4)~(6). In order to demonstrate the system performance, intensity derived from the polarimeter and that from the original PSF are measured and compared. The experimental procedure is shown in Fig. 3.

3.2 Results and analyses

Figure 4 shows measured intensities (I_L and I_R) plotted in logarithmic coordinates when half-wave plate axis oriented at 0° and 22.5° respectively, and diffraction patterns can be clearly observed.

Before the optimization, initial values of g_1~g_5 are set to 0, and x_0, y_0 and s are set to 10, 10 and 1, respectively. Then the optimization process is executed, and relationships between optimization steps and values of the objective functions for the Q and U components are shown in

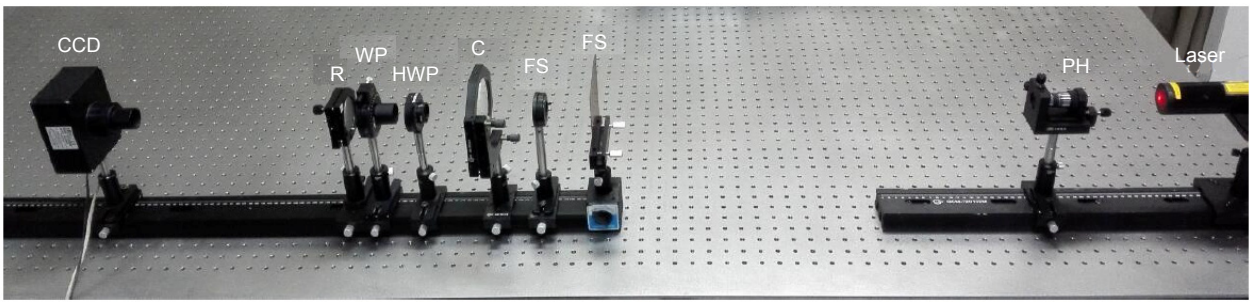

Fig. 2 Experimental setup of the differential-imaging polarimeter. PH: pinhole. FS: field stop. C: collimator lens. HWP: half-wave plate. WP: Wollaston prism. R: re-imaging lens. CCD: charge-coupled device.

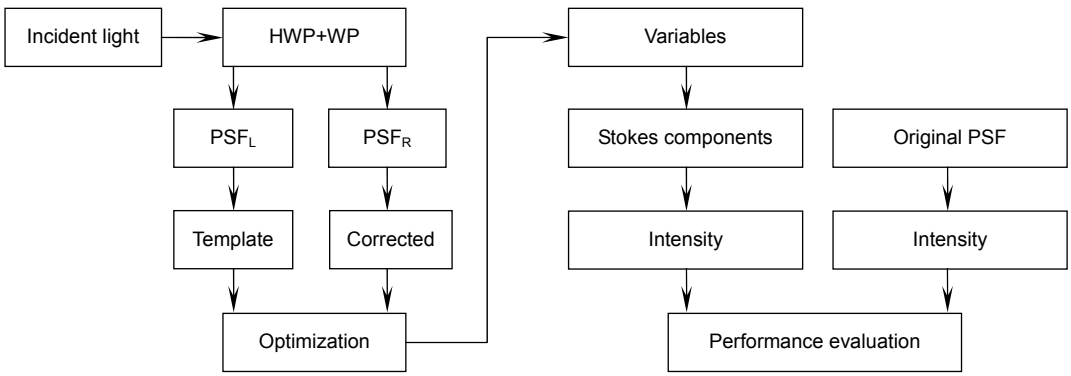

Fig. 3 Flow chart of the experiment.

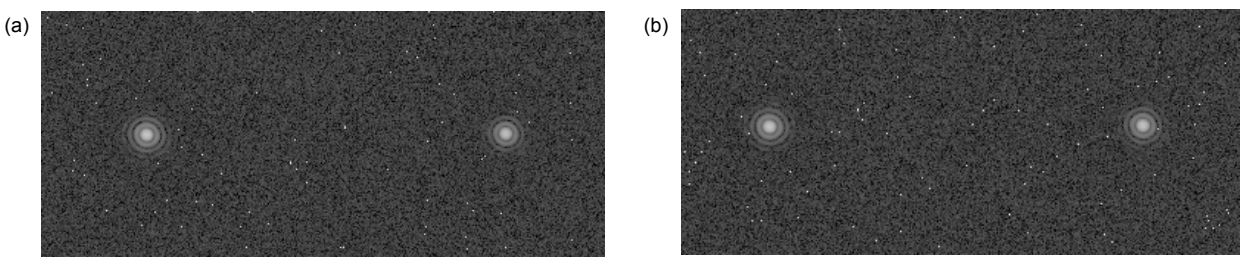

Fig. 4 Measured intensities in logarithmic coordinates. (a) HWP@0° for the Q component. (b) HWP@22.5° for the U component .

Fig. 5.

Figure 5 shows that value of the objective function for the Q component and U component decreased rapidly before around 90 and 120 steps, respectively, and then it gradually dropped to 3.11×10^6 and 3.97×10^6, and total optimization steps for the two components are 1085 and 893, respectively. After the optimization, eight optimized parameters for the Q and the U components are shown in Table 1.

Figure 6 shows polarized components after optimization and subtraction as well as measured intensity of the original PSF. The results are plotted within an angular distance of $9\lambda/D$. Fig. 6 reveals that the unpolarized starlight can be effectively suppressed by the polarimetry approach. Compared with the original PSF, intensities of both Q and U components are much smaller, and an extra contrast improvement of about 30~50 in the region $3\lambda/D$~$5\lambda/D$ is achieved. Due to the noise (such as detector's readout noise: 15 electrons) becomes relatively larger with increasing separation from the light spot center, the diffraction pattern beyond an angular distance of $8\lambda/D$ is not obvious in the original PSF. However, the contrast improvement throughout the region of small angular distance by the polarimeter is apparent. The experimental

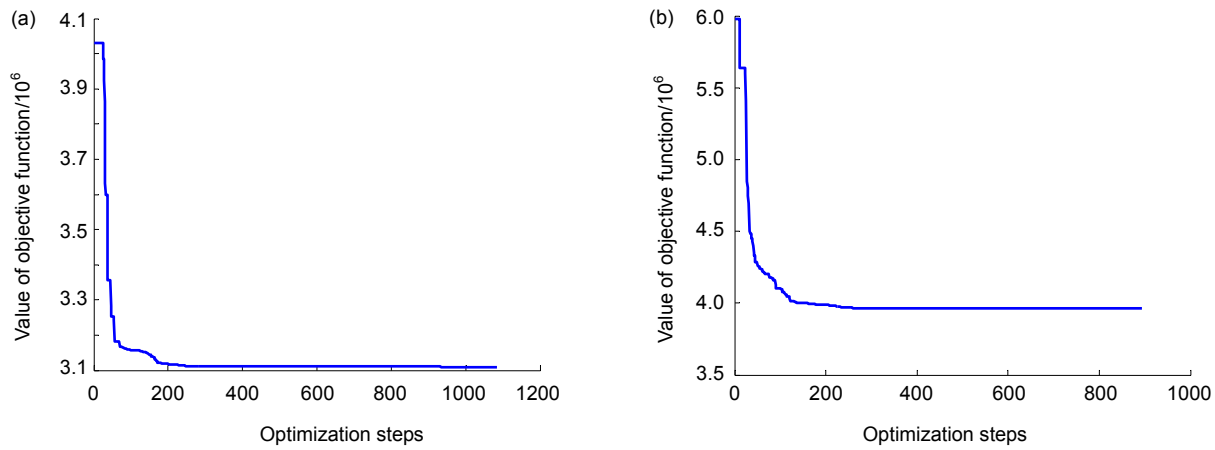

Fig. 5 Optimization curve. (a) Value of objective function of the Q component. (b) Value of objective function of the U component.

Table 1 Values of the parameters determined in the optimization.

	g_1	g_2	g_3	g_4	g_5	x_0	y_0	s
Initial value	0	0	0	0	0	10	10	1
Optimized for Q component	-1.779×10^{-5}	-4.373×10^{-6}	1.296×10^{-5}	8.118×10^{-6}	-4.343×10^{-9}	4.34	3.09	0.997
Optimized for U component	-8.155×10^{-6}	-3.964×10^{-7}	1.042×10^{-5}	-5.967×10^{-5}	8.624×10^{-8}	9.939	10.064	1.025

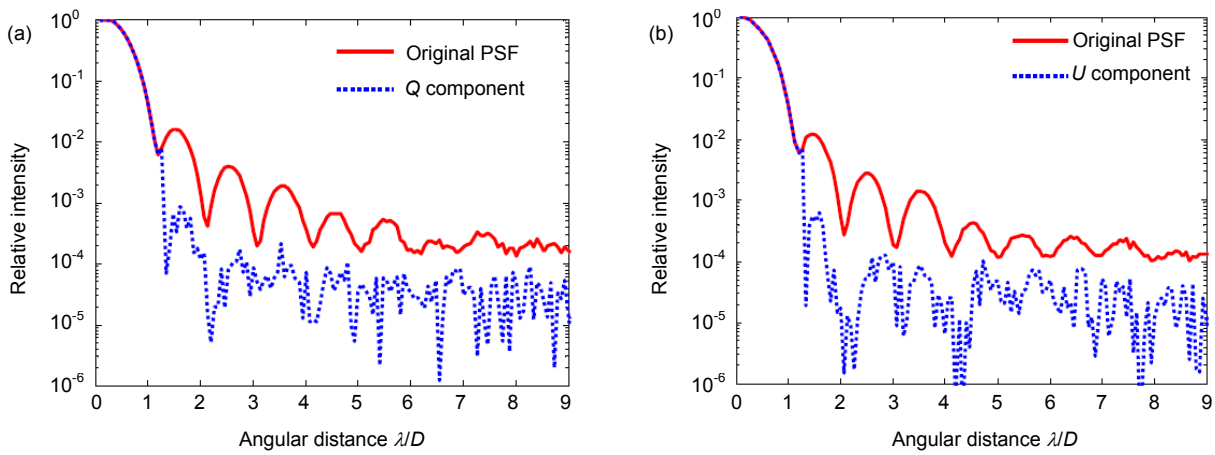

Fig. 6 Intensity comparisons. (a) The original PSF and Q component. (b) The original PSF and U component.

results demonstrate that our polarimeter works well for both perpendicular polarization components. It is worth noting that the polarimetric performance is also affected by several other factors, e.g. azimuth error of rotatable elements, retardance accuracy of the HWP, and instrumental polarization. Therefore, we believe that better performance can be achieved, if high-quality polarization elements and lower noise camera are used.

4 Conclusions

In this paper, we presented a simple but robust polarimeter: a differential-imaging polarimeter, which deploys a half-wave plate and a Wollaston prism, and uses an eight-variable optimization algorithm for best performance. Our polarimeter has the following advantages: 1) the system is simple and compact, which is different from the traditional polarimeter that employs the mechanical modulation approach; 2) image distortion and intensity unbalance are considered and are optimized for best contrast performance; 3) most important, each polarization component is measurement simultaneously, which is fundamentally immune to the rapidly-changed atmospheric turbulence induced speckle noise. Laboratory experiments indicate that the proposed polarimeter combined with the optimization algorithm successfully achieved an extra contrast of ~30~50 times in a close angular distance in the region of $3\lambda/D$~$5\lambda/D$. The work demonstrated in this paper is a promising technique, since our polarimeter has the potential to achieve an overall contrast better than 10^{-8} when used with current extreme adaptive optics and coronagraph systems, and such work is critical to achieve the scientific goal toward the direct imaging of giant Jupiter-like exoplanets for a ground-based telescope.

Finally, our optimization algorithm is achieved for the minimum starlight PSF intensity, which makes our polarimeter suitable for both unpolarized and polarized starlight. For future works, we will update the polarimeter with a low readout-noise scientific CMOS camera manufactured by PCO (PCO edge 5.5, with a readout noise of 1.4 electrons), and phase correction will also be included. Further related progress will be discussed in a future publication.

Acknowledgements

This work was funded by the National Natural Science Foundation of China (NSFC, 11703058, 11703056, 11661161011, 11433007, 11220101001, 11328302, 11373005 and 11303064), the Opening Project of Key Laboratory of Astronomical Optics & Technology, Nanjing Institute of Astronomical Optics & Technology, Chinese Academy of Sciences (CASKLAOT-KF201606), the "Strategic Priority Research Program" of the Chinese Academy of Sciences (XDA04075200), the Special Fund for astronomy of CAS (2015–2016), the Special Fund for Young Researcher of Nanjing Institute of Astronomical Optics & Technology, the International Partnership Program of the Chinese Academy of Sciences (114A32KYSB20160018). Some of this work was carried out at California State University Northridge with the support from NSF AST-1607921, and the Mt. Cuba Astronomical Foundation.

References

1 Santos N C, Bouchy F, Mayor M, *et al*. The HARPS survey for southern extra–solar planets II. A 14 Earth–masses exoplanet around μ Arae[J]. *Astronomy and Astrophysics*, 2004, **426**(1): L19–L23.

2 Narayan R, Cumming A, Lin D N C. Radial velocity detectability of low–mass extrasolar planets in close orbits[J]. *The Astrophysical Journal*, 2005, **620**(2): 1002–1009.

3 Borucki W, Koch D, Batalha N, *et al*. KEPLER: Search for Earth–size planets in the Habitable Zone[C]//Transiting Planets, Proceedings of the International Astronomical Union, 2009, **253**: 289–299.

4 Pepe F, Ehrenreich D, Meyer M R. Instrumentation for the detection and characterization of exoplanets[J]. *Nature*, 2014, **513**(7518): 358–366.

5 Soummer R, Aime C, Falloon P E. Stellar coronagraphy with prolate apodized circular apertures[J]. *Astronomy & Astrophysics*, 2003, **397**(3): 1161–1172.

6 Kasdin N J, Vanderbei R J, Spergel D N, *et al*. Extrasolar planet finding via optimal apodized–pupil and shaped–pupil coronagraphs[J]. *The Astrophysical Journal*, 2003, **582**(2): 1147–1161.

7 Guyon O, Pluzhnik E A, Kuchner M J, *et al*. Theoretical limits on extrasolar terrestrial planet detection with coronagraphs[J]. *Astrophysical Journal Supplement Series*, 2006, **167**(1): 81–99.

8 Bordé P J, Traub W A. High–contrast imaging from space: speckle nulling in a low–aberration regime[J]. *The Astrophysical Journal*, 2006, **638**(1): 488–498.

9 Ren D Q, Zhu Y T. A coronagraph based on stepped–transmission filters[J]. *Publications of the Astronomical Society of the Pacific*, 2007, **119**(859): 1063–1068.

10 Liu C C, Ren D Q, Dou J P, *et al*. A high–contrast coronagraph for direct imaging of Earth–like exoplanets: design and test[J]. *Research in Astronomy and Astrophysics*, 2015, **15**(3): 453–460.

11 Dou J P, Ren D Q. Phase quantization study of spatial light modulator for extreme high contrast imaging[J]. *The Astrophysical Journal*, 2016, **832**(84): 1–11.

12 Trauger J T, Traub, W A. A laboratory demonstration of the capability to image an Earth–like extrasolar planet[J]. *Nature*, 2007, **446**(7137): 771–773.

13 Kay J D, Pueyo L A, Kasdin N J. Demonstration of a symmetric dark hole with astroke–minimizing correction algorithm[J]. *Proceedings of SPIE*, 2009, **7209**: 72090G.

14 McBride J, Graham J R, Macintosh B, *et al*. Experimental design for the Gemini planet imager[J]. *Publications of the Astronomical Society of the Pacific*, 2011, **123**: 692–708.

15 Seager S, Whitney B A, Sasselov D D. Photometric light curves and polarization of close–in extrasolar giant planets[J]. *The Astrophysical Journal*, 2000, **540**(1): 504–520.

16 Saar S H, Seager S. Uses of linear polarization as a probe of extrasolar planet atmospheres[C]//*ASP Conference Series*, 2003, **294**: 529–534.
17 Stam D M, Hovenier J W, Waters L B F M. Using polarimetry to detect and characterize Jupiter–like extrasolar planets[J]. *Astronomy & Astrophysics*, 2004, **428**(2): 663–672.
18 Berdyugina S V, Berdyugin A, Fluri D M, *et al*. Polarized reflected light from the exoplanet HD 189733b: first multicolor observations and confirmation of detection[J]. *The Astrophysical Journal Letters* , 2011, **728**(1): L6.
19 Hough J H, Lucas P W, Bailey J A, *et al*. PlanetPol: a very high sensitivity polarimeter[J]. *Publications of the Astronomical Society of the Pacific*, 2006, **118**(847): 1302–1318.
20 Perrin M D, Graham J R, Lloyd J P. The IRCAL polarimeter: design, calibration, and data reduction for an adaptive optics imaging polarimeter[J]. *Publications of the Astronomical Society of the Pacific*, 2008, **120**(867): 555–570.
21 Hinkley S, Oppenheimer B R, Soummer R, *et al*. Speckle suppression through dual imaging polarimetry, and a ground–based image of the HR 4796A circumstellar disk[J]. *The Astrophysical Journal*, 2009, **701**(1): 804–810.
22 Perrin M D, Graham J R, Larkin J E, *et al*. Imaging polarimetry with the Gemini planet imager[J]. *Proceedings of SPIE*, 2010, **7736**: 77365R.
23 Dou J P, Ren D Q, Zhu Y T, *et al*. Laboratory test of a polarimetry imaging subtraction system for the high–contrast imaging[J]. *Proceedings of SPIE*, 2012, **8446**: 84468D.
24 Liu C C, Ren D Q, Zhu Y T, *et al*. A high–contrast imaging polarimeter with a stepped–transmission filter based coronagraph[J]. *Research in Astronomy and Astrophysics*, 2016, **16**(5): 27-32.
25 Roelfsema R, Schmid H M, Pragt J, *et al*. The ZIMPOL high–contrast imaging polarimeter for SPHERE: design, manufacturing, and testing[J]. *Proceedings of SPIE*, 2010, **7735**: 77354B.
26 Perrin M D, Duchene G, Fitzgerald M P, *et al*. Gemini planet imager polarimetry of the circumstellar ring around HR 4796A[C]// *American Astronomical Society*, 2015, **225**: 330.05.
27 Burrows A. A theoretical look at the direct detection of giant planets outside the Solar System[J]. *Nature*, 2005, **433**(7023): 261–268.
28 Burrows A, Sudarsky D, Hubeny I. Spectra and diagnostics for the direct detection of wide–separation extrasolar giant planets[J]. *The Astrophysical Journal*, 2004, **609**(1): 407–416.
29 Macintosh B A, Anthony A, Atwood J, *et al*. The Gemini Planet Imager: integration and status[J]. *Proceedings of SPIE*, 2012, **8446**: 84461U.
30 Carbillet M, Bendjoya P, Abe L, *et al*. Apodized Lyot coronagraph for SPHERE/VLT. I. Detailed numerical study[J]. *Experimental Astronomy*, 2011, **30**(1): 39–58.
31 Currie T, Guyon O, Martinache F, *et al*. The Subaru coronagraphic extreme adaptive optics imager: first results and on–aky performance[C]//*Proceedings of the International Astronomical Union*, 2013, **299**: 1307.
32 Macintosh B A, Graham J R, Palmer D W, *et al*. The Gemini Planet Imager: from science to design to construction[J]. *Proceedings of SPIE*, 2008, **7015**: 701518.
33 Martinez P, Carpentier E A, Kasper M. Laboratory demonstration of efficient XAO Coronagraphy in the context of SPHERE[J]. *Publications of the Astronomical Society of the Pacific*, 2010, **122**: 916–923.
34 Wang X, Ren D Q, Dou J P, *et al*. A dual–channel imaging polarimetry system[J]. *Proceedings of SPIE*, 2011, **8197**: 81971I.
35 Dou J P, Ren D Q, Zhu Y T, *et al*. A demonstration test of the dual–beam polarimetry differential imaging system for the high–contrast observation[J]. *Proceedings of SPIE*, 2012, **8446**: 84461X.
36 Weng J, Cohen P, Herniou M. Camera calibration with distortion models and accuracy evaluation[J]. *IEEE Transactions on Pattern Analysis and Machine Intelligence*, 1992, **14**(10): 965–980.
37 Tamaki T, Yamamura T, Ohnishi N. Correcting distortion of image by image registration[J]. *International Journal of Image and Graphics*, 2002, **2**(2): 309-329.
38 El-Melegy M T, Farag A A. Nonmetric lens distortion calibration: closed–form solution, robust estimation and model selection[C]//*Ninth IEEE International Conference on Computer Vision*, 2003, Nice, France, France: IEEE 2003, **2**: 554–559.
39 Macintosh B A, Anthony A, Atwood J, *et al*. The Gemini planet imager: first light and commissioning[J]. *Proceedings of SPIE*, 2014, **9148**: 91480J.
40 Canovas H, Rodenhuis M, Jeffers S V, *et al*. Data–reduction techniques for high–contrast imaging polarimetry Applications to ExPo[J]. *Astronomy & Astrophysics*, 2011, **531**: A102.

.